Nanoscale

PAPER

View Article Online
View Journal | View Issue

Bottom-up synthesis of nitrogen-doped graphene sheets for ultrafast lithium storage

Cite this: *Nanoscale*, 2014, **6**, 6075

Lei-Lei Tian,[ab] Xian-Yong Wei,*[a] Quan-Chao Zhuang,*[b] Chen-Hui Jiang,[b] Chao Wu,[ab] Guang-Yao Ma,[b] Xing Zhao,[ab] Zhi-Min Zong[a] and Shi-Gang Sun[c]

Received 23rd January 2014
Accepted 21st March 2014

DOI: 10.1039/c4nr00454j

www.rsc.org/nanoscale

A facile bottom-up strategy was developed to fabricate nitrogen-doped graphene sheets (NGSs) from glucose using a sacrificial template synthesis method. Three main types of nitrogen dopants (pyridinic, pyrrolic and graphitic nitrogens) were introduced into the graphene lattice, and an inimitable microporous structure of NGS with a high specific surface area of 504 m^2 g^{-1} was obtained. Particularly, with hybrid features of lithium ion batteries and Faradic capacitors at a low rate and features of Faradic capacitors at a high rate, the NGS presents a superior lithium storage performance. During electrochemical cycling, the NGS electrode afforded an enhanced reversible capacity of 832.4 mA h g^{-1} at 100 mA g^{-1} and an excellent cycling stability of 750.7 mA h g^{-1} after 108 discharge–charge cycles. Furthermore, an astonishing rate capability of 333 mA h g^{-1} at 10 000 mA g^{-1} and a high rate cycle performance of 280.6 mA h g^{-1} even after 1200 cycles were also achieved, highlighting the significance of nitrogen doping on the maximum utilization of graphene-based materials for advanced lithium storage.

1 Introduction

To design advanced energy storage devices, electrode materials with both high energy and high power density are urgently and essentially needed. Hence it is required to incorporate the features of supercapacitors with high rate performance and rechargeable batteries with high energy densities into a single unit.[1] Graphene, defined as a monolayer of sp^2-hybridized carbon atoms arranged in a honeycomb lattice, has become one of the most exciting materials in recent years.[2,3] By virtue of its extraordinary physicochemical properties, including large surface area, high conductivity, structural flexibility and chemical stability, graphene has been intensively explored as an electrode material and/or a substrate of hybrid materials for high performance lithium ion batteries (LIBs).[4–14] It is commonly estimated that graphene might be more suitable for reversible lithium storage than commercial bulk graphite, because the graphene sheets could double the sorption capacity by binding the lithium ion on both sides of the graphene plane and by shortening the lithium diffusion distance.[4,5,15–20] However, it is recently concluded that the lithium coverage on the surface of single layer graphene is actually smaller, because of the lower binding energies of lithium to carbon and the strong Coulombic repulsion of the lithium atoms on the opposite sides of graphene as well as the small charge transfer between lithium and graphene.[16,21,22] Moreover, the Li^+ diffusion parallel to the graphene planes is seriously hindered by the higher diffusion barrier resulting from the accumulated Li^+ in large area multilayer graphene (MLG).[23]

Fortunately, heteroatomic dopants could substantially increase the lithium storage performance of carbon materials.[24] Nitrogen is one of the most attractive modification dopants because its electronegativity is higher than that of carbon and its atomic diameter is close to that of carbon.[25–33] The enhanced binding interactions between nitrogen dopants and lithium might sharply increase the lithium coverage of the graphene layer.[25,34] In addition, appropriate incorporation of nitrogen in graphitic networks could boost the electronic conductivity and reversibly cycle lithium ions.[34–36] Furthermore, along with nitrogen dopants, considerable defects were also introduced, which could lower the diffusion barriers and thus facilitate the Li^+ diffusion through/across the graphene layers.[23] Nitrogen-doped graphene has been hitherto fabricated through two main routes:[37] one is direct synthesis, including chemical vapor deposition (CVD),[27–29] solvothermal synthesis,[33] *etc.*, and the other is post-treatment doping, such as fumigation in NH_3,[24,30–32,38] plasma treatment,[39,40] hydrazine hydrate treatment,[41,42] *etc.* However, most of these methods are complicated and cannot achieve homogeneous nitrogen doping with a high nitrogen content.

Herein, we report a facile bottom-up strategy to fabricate nitrogen-doped graphene sheets (NGSs) as ultrafast lithium

[a]*School of Chemical Engineering and Technology, China University of Mining & Technology, Xuzhou 221116, China. E-mail: wei_xianyong@163.com; Fax: +86 516 83591870; Tel: +86 516 83591877*

[b]*School of Materials Science and Engineering, China University of Mining & Technology, Xuzhou 221116, China. E-mail: zhuangquanchao@126.com*

[c]*State Key Laboratory of Physical Chemistry of Solid Surfaces, Department of Chemistry, College of Chemistry and Chemical Engineering, Xiamen University, Xiamen 361005, China*

storage materials for advanced LIBs. During the sacrificial template synthesis process, the mixture of glucose and dicyandiamide was first thermally polymerized to create layered stacks of the graphitic carbon nitride (GCN, g-C_3N_4) template, and aromatic carbon intermediates were enclosed within the interlayer gaps of GCN simultaneously. The NGS with microporous nanoarchitecture was finally achieved when the GCN template undergoes thermolysis. The unique microporous nanoarchitecture could efficiently increase the interfacial interaction and improve Li^+ diffusion. During the electrochemical cycles, the NGS could store lithium with hybrid features of LIBs and Faradic capacitors at a low rate and features of Faradic capacitors at a high rate, and thus afforded enhanced reversible capacity, excellent cycling stability as well as superior rate capability.

2 Experimental section

2.1 Synthesis of NGS

Dicyandiamide (DCDA, 99.5%), monohydrate glucose (MHG) and anhydrous ethanol (AHE) were used without further purification. In a typical synthesis, appropriate amounts of DCDA, MHG and AHE were poured into a milling pot, in which the mass ratio of DCDA to MHG was fixed to 10. The mixture was mixed for 4 h using a planet type ball mill, and then dried. Subsequently, the obtained powder of the precursor was heated in two steps under a nitrogen atmosphere. In the low-temperature state, the precursor was heated to 580 °C at 2.2 °C min^{-1} and kept at this temperature for 4 h.[43,44] DCDA was pyrolyzed during this step to create layered stacks of the GCN template, and the aromatic carbon intermediates resulting from MHG were enclosed within the interlayer gaps of GCN (denoted as GCN enclosed graphene, GEG). The NGS was finally obtained after removing the GCN template from GEG by thermolysis at 800 °C for 2 h, and MLG was contrastively prepared by heating the GEG at 1000 °C for 2 h. As a reference, graphene nanosheets (GNSs) were also synthesized using the typical method of reducing exfoliated graphite oxides.[45]

2.2 Material characterization

Scanning electron microscopy (SEM) characterization was performed on a field emission JSM-6700F instrument, and transmission electron microscopy (TEM) image was captured on a JEOL-2010 instrument at an acceleration voltage of 200 kV. Elemental mapping images of NGSs were scanned using energy filtered TEM (EFTEM, JEM-ARM200F). In order to reveal the changes that occurred during heat treatment at the high-temperature state, TG analysis for GEG, NGS and MLG were carried out with a Q5000 IR Thermogravimetric Analyzer (TGA, TA Instruments), in which the dried material was heated in a nitrogen atmosphere at 10 °C min^{-1} from room temperature to 1000 °C. To evaluate the structural changes of GEG to NGS and MLG, X-ray diffraction (XRD) measurements were analyzed with Cu Kα radiation at $\lambda = 1.054$ Å on a Bruker AXS D8 X-ray diffractometer. The surface area and porosity were measured from the standard nitrogen adsorption isotherms at 77 K using an automated Micropore gas analyzer Autosorb-1 MP (Quantachrome Instruments) and data analysis was performed with Quantachrome software. Furthermore, the crystallographic structure of the materials was determined using a Bruker AXS D8 X-ray diffractometer with Cu Kα radiation. X-ray photoelectron spectroscopy (XPS) (ESCALAB 250 Xi; Al anode X-ray source) was used to investigate the surface chemistries of the obtained material, and the Raman spectra were obtained with a high-resolution, dispersive Raman spectrometer system (Horiba-Jobin Yvon LabRam HR) equipped with a visible laser excitation of 514 nm.

2.3 Electrochemical test

The working electrodes were prepared by spreading a mixture of active mass (80 wt% for NGS, MLG and GNS electrodes, respectively and 60 wt% for the GEG electrode), acetylene black (only added for the GEG electrode, 20 wt%) and polyvinylidene fluoride (Kynar FLEX 910, Elf Atochem) binder dissolved in *N*-methylpyrrolidone (Fluka Inc., St. Louis, MO, USA) onto a Cu foil (thickness 20 μm) current collector. The electrolyte consists of 1 M $LiPF_6$ in a mixture of isometric ethylene carbonate, dimethyl carbonate, and diethyl carbonate (Guotai-Huarong Co., Zhangjiagang, China). The electrochemical characterisations were conducted in 2025-type coin cells using Li foil (99.9%, China Energy Lithium Co., Ltd., Tianjin) as the counter electrode. Galvanostatic charge–discharge (GCD) experiments were conducted on a battery testing system (CT2001A, Land) over a range of 0.01–3 V *vs.* Li/Li^+. Cyclic voltammetry (CV) measurements were performed on an electrochemical workstation (Ivium Stat) within the range of 0–3 V. The reported specific capacities (SCs) are all normalized to the weight of active materials.

3 Results and discussion

To investigate the morphology and microstructure of the products, optical photographs, SEM and TEM images were taken from the as-prepared materials. As shown in Fig. 1, different from the conventional brilliant yellow[44] of GCN (Fig. 1a), GEG appeared as grayish-black bulk. The representative SEM image shows that the GEG consists of dense agglomerates with a size of several micrometers. After heating the GEG at 800 °C, "silk like" NGSs were obtained without the presence of any residual GCN. According to the SEM and TEM images, the freestanding graphene sheets display a layered morphology, intrinsic microscopic roughening and out-of-plane deformations for both NGSs and MLG. Compared with the rich thick nanosheet of MLG, the NGSs display a vague and very flexible appearance with a typical waving, indicating the sparing restacking of graphene layers in NGSs. The microstructures of individual NGS were further examined by EFTEM and high-resolution TEM (HRTEM). As shown in Fig. 2a–d, there is a uniform distribution of C, N and O elements throughout the graphene sheet. From these qualitative observations, the dense agglomerated GCN was significantly detracted, and thus the nitrogen dopant has been evenly inserted into the graphene

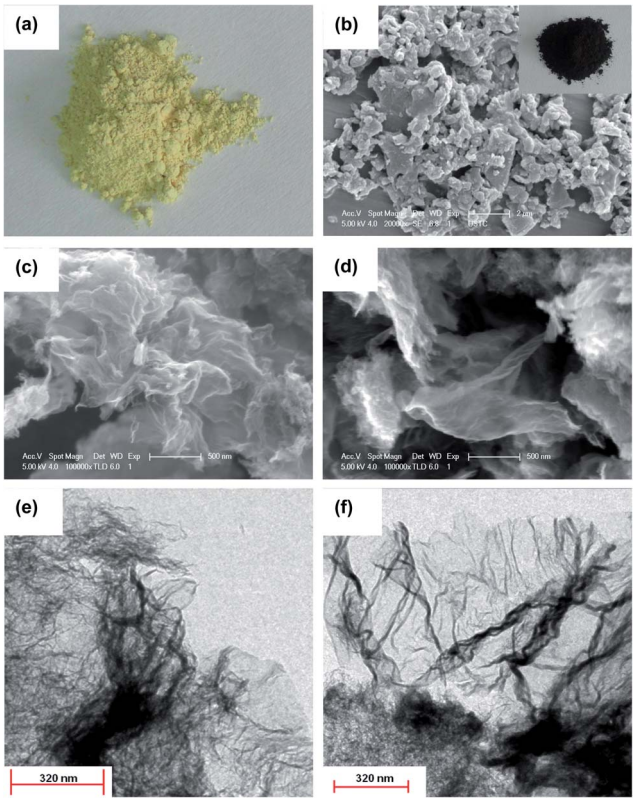

Fig. 1 (a) Optical image of GCN, (b) SEM image of GEG (the inset shows the optical image), representative SEM and TEM images of (c and e) NGS and (d and f) MLG.

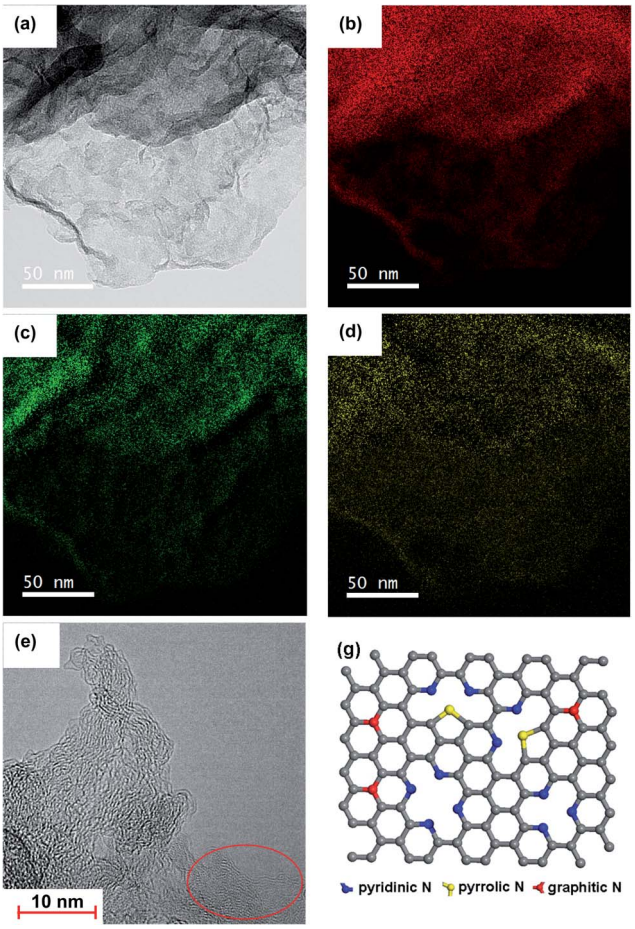

Fig. 2 EFTEM elemental mapping and HRTEM images of a single NGS. (a) Zero-loss image, (b) C–K mapping, (c) N–K mapping, (d) O–K mapping, (e) HRTEM image. (g) Schematic representation of nitrogen-doped graphene.

basal plane. The HRTEM image (Fig. 2e) displays the honeycomb-like molecular structure of the single nitrogen-doped graphene sheet; the more irregular domains confirm the defects and/or functional groups in the NGS basal plane.

The TG curve of GEG (Fig. 3a) shows two weight loss (WL) steps. The first one is prior to 200 °C with a WL of 4.56% and could be attributed to the evaporation of the absorbed moisture.[46] The major part of the WL seems to occur at *ca.* 689 °C and the rapid WL of 90.53% was mainly caused by the pyrolysis of the GCN template,[43,47] whereas the TG curves of both NGS and MLG (Fig. 3b and c) show three WL steps. Prior to 100 °C, the rapid WL came from the desorption of free water in the graphene layers. The WL in the temperature range of 230–450 °C was predominantly caused by the elimination of organic residues in the samples. The major part of the WL occurred above 600 °C, corresponding to the pyrolysis of functional groups and/or residual GCN. While the WL of 2.1% occurred for MLG, the WL for NGS is 22.1%, indicating that the nitrogen dopants decomposed almost completely at 1000 °C. According to the TG results, the mass ratios of the nitrogen components in the NGS and MLG are *ca.* 23.6% and 2.1%, respectively. In addition, the WL of absorbed free water below 100 °C for the NGS (*ca.* 6.4%) is more obvious than that for MLG (*ca.* 1.3%), indicating the developed absorptive abilities as well as the enlarged surface area of the NGS.

The structure of the GCN can be considered as graphite-like single layers aligning with each other along the hexagonal

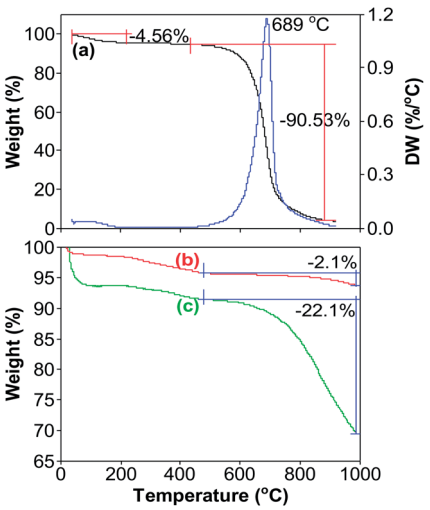

Fig. 3 TG results of (a) GEG, (b) MLG and (c) NGS. DW denotes differential weight.

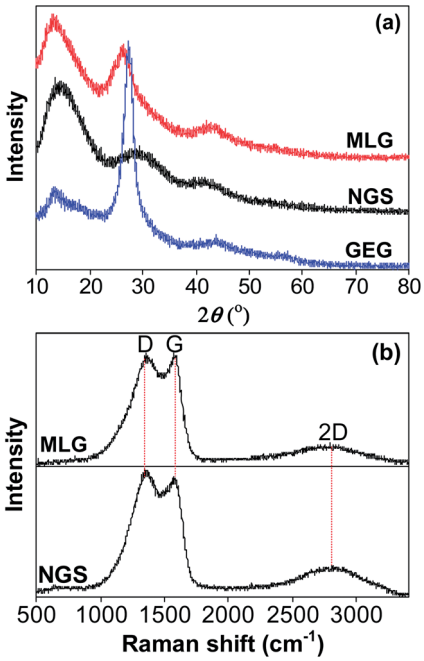

Fig. 4 (a) XRD patterns of GEG, MLG and NGS, and (b) Raman spectra of NGS and MLG.

c-axis. As shown in Fig. 4a, GEG has two diffraction peaks in consistence with the GCN.[48–50] The low-angle peak at 13.1° can be attributed to an in-plane structural packing motif, for example, the hole-to-hole distance of the nitride pores.[49] The strong and sharp peak at 27.4° can be indexed as the (002) plane of the GCN, corresponding to the interlayer *d*-spacing of 0.325 nm.[44,48,50] Nevertheless, the peak around 27.4° in the XRD pattern of NGSs was largely weakened and broadened, which can be attributed to the presence of intercalated "N defects" in the low-crystallized graphene plane.[47,51] Because the graphitic structure of GCN was thoroughly wrecked after the pyrolysis at 800 °C, the much amplified peak around 13.1° should be attributed to the layered structure of NGSs, corresponding to the interlamellar distance of 0.62 nm. It suggests that there could be some nitrogen groups propping out of the graphene plane besides the in-plane nitrogen dopants. These nitrogen groups could practically prevent the restacking of graphene layers and maintain the large interlayer distance, and thus increasing the interfacial interaction of NGSs and improving the diffusion of the lithium ion between graphene layers. The enhanced (002) peak of MLG, as well as the (100) peak (around 42.5°), confirmed a certain restacking of the un-propped graphene sheets after oversintering. In accordance with the above analyses, Raman analysis could also provide convincing evidence of the NGS and the restacked MLG. As shown in Fig. 4b, the Raman spectra of the NGS and MLG exhibit two high intensity peaks around 1360 cm^{-1} (D band) and 1580 cm^{-1} (G band). The G band characteristic of the in-plane vibration from a layer of sp^2-hybridized carbon atoms provides the formation of graphitic carbon in both NGS and MLG, while the D band could be attributed to the defects or imperfections, reflecting the presence of disorder and the edges and boundaries of the graphene domains.[43,52] Crucially, however, the D/G intensity ratio ($I_D/I_G = 1.06$) in the NGS is slightly larger than that ($I_D/I_G = 1$) in MLG, suggesting a relatively larger number of defects and disordered edge sites in the NGS.[53] Furthermore, the enhanced 2D band around 2800 cm^{-1} in the Raman spectra of the NGS manifests a less number of layers of the graphene nanosheet in the NGS.[52]

The specific surface area (SSA) and porous structure characteristics of the NGS, MLG and GNS were investigated by nitrogen isothermal adsorption, as shown in Fig. 5a. Compared with the type H2 IUPAC (International Union of Pure and Applied Chemistry) loop of the GNS, hysteresis loops of both NGS and MLG resemble the type H3 classification, corresponding to the sheet particles or slit-shaped pores between parallel graphene sheets in the NGS and MLG.[54] Somewhat differently, the hysteresis loop of the NGS appeared at a lower relative pressure (RP) far from 0.4 (near 0.05), which is much lower than that of MLG (appeared at *ca.* 0.45 of RP), indicating the presence of a considerable amount of longer slit-shaped microporosity in NGS. The SSA and total pore volume (TPV) of the NGS are 504 $m^2\ g^{-1}$ and 0.96 $cm^3\ g^{-1}$, respectively, being significantly higher than those of the GNS (483 $m^2\ g^{-1}$ and 0.70 $cm^3\ g^{-1}$) (Table 1). In contrast, the SSA and TPV of MLG are only 241 $m^2\ g^{-1}$ and 0.55 $cm^3\ g^{-1}$, respectively, indicating a very low micropore content, which can be attributed to the restacking of graphene layers after the elimination of nitrogen dopants when over-calcined at a higher temperature. The corresponding porosity distribution in Fig. 5b shows the dominant presence of microporosities and a few mesoporosities in both NGS and MLG. Prevailing porosities with a radius of *ca.* 0.36 nm might conform to the slit-shaped microporosities enclosed by in-plane monovacancies (and/or divacancies) and graphene layers,[23] the

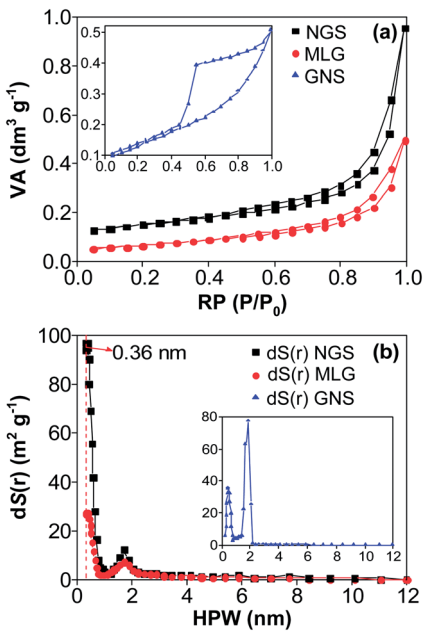

Fig. 5 (a) Nitrogen adsorption–desorption isotherms and (b) the corresponding porosity distribution of the NGS, MLG and GNS. VA and HPW denote the volume adsorbed and half pore width, respectively.

Table 1 BET surface areas and cumulative pore volume of the NGS, MLG and GNS obtained from nitrogen adsorption isotherms at 77 K

Sample	SSA (m^2 g^{-1})	TPV (cm^3 g^{-1})
NGS	504	0.96
MLG	241	0.55
GNS	483	0.70

Table 2 Surface atomic percentages of C, N and O in the NGS, MLG and GNS determined by XPS

Sample	C 1s	N 1s	O 1s
NGS	74.74	19.46	5.80
MLG	90.05	6.20	3.75
GNS	93.52	2.04	4.44

mesoporosities with a radius of *ca.* 1.7 nm could be analogous to the intergranular cavities in the graphene plane.[43] It is evident that the differential pore area [d$S(r)$] peak at a radius of 0.36 nm in MLG is largely decreased, showing the decline of in-plane monovacancies with the elimination of the nitrogen dopants.

As presented in Fig. 6, signals of elements C, N, and O are displayed in the wide XPS spectrum survey and the sharp C 1s peak manifests the graphene lattices. As shown in Table 2, the nitrogen atomic percentage in the NGS is 19.46%, which is much higher than that in MLG and GNS, revealing the presence of nitrogen dopants in the NGS. The high-resolution spectra were taken on the C 1s and N 1s regions and could be deconvoluted into various components. Different from the sharp C 1s peak (Fig. 6d) of GNS, the broad NGS C 1s spectra in Fig. 6b can be resolved into four peaks with binding energies of 284.9, 285.7, 286.2 and 288 eV, respectively. The primary peak at 284.9 eV is typically assigned to graphitic carbon in the literature,[29] but can also be attributed to sp2 C–N.[55] The peak at 288 eV is identified as sp^2-hybridized carbon in the aromatic ring attached to the nitrogen groups, and the peaks at 285.7 and 286.2 eV correspond to C–N and C–O/C=N, respectively.[29,32,56] However, the peak at 286.2 eV disappeared in MLG C 1s spectra (Fig. 6c), and a new peak at 290.3 eV emerged, indicating the transformation of hydroxyls to carboxylate carbon (O–C=O).[57] The N 1s spectra of the NGS (Fig. 6e) reveales three major components corresponding to pyridinic nitrogen (398.46 eV), pyrrolic nitrogen (400.17 eV) and graphitic nitrogen (N–(C)3, 401.2 eV), respectively.[32,46,55,58–60] According to the report by Thomas A. *et al.*,[59] GCN could transform into cyano fragments and nitrogen when heated to 700 °C. It is speculated that nitrogen might be introduced into the graphene lattice by the electrophilic substitution reaction between cyano fragments and actived carbon atoms in graphene. Signals of pyrrolic nitrogen in the N 1s spectra of MLG could not be detected, and the peaks of pyridinic nitrogen and graphitic nitrogen were significantly weakened, indicating the elimination of nitrogen dopants in MLG after postannealing.

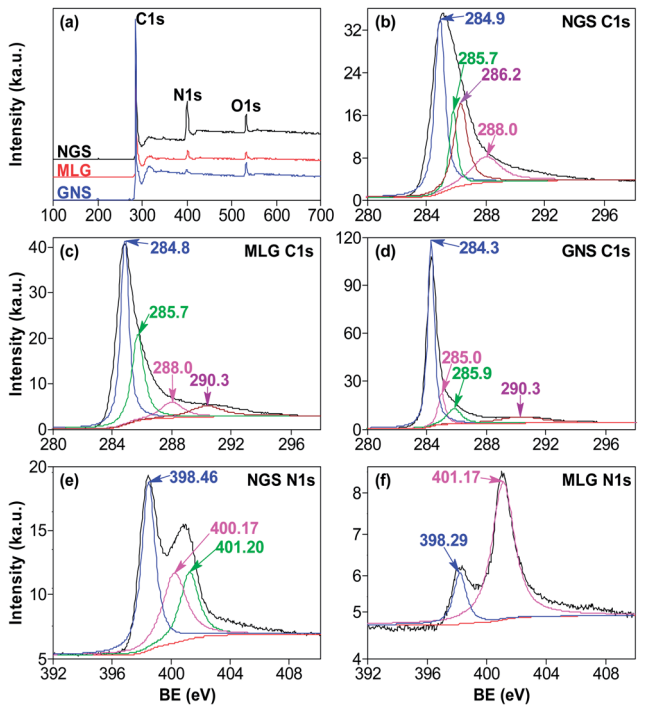

Fig. 6 XPS survey spectra of graphene synthesized by the sacrificial template strategy and reducing exfoliated graphite oxides method. (a) Wide XPS spectra of the NGS, MLG, and GNS, (b) high-resolution XPS C 1s spectra and their fitting results of the NGS, (c) MLG and (d) GNS, and (e) high-resolution XPS N 1s spectra and their fitting results of NGS and (f) MLG. BE denotes binding energy.

The electrochemical performances of the as-prepared materials were firstly evaluated by using galvanostatic charge–discharge measurements at a current density of 100 mA g^{-1} over the voltage range 0.05–3.0 V *vs.* Li/Li^+. Fig. 7a–d show the 1st, 2nd, 50th and 100th charge–discharge curves and cyclic performances of the NGS, MLG, GEG and GNS electrodes. The first cycle discharge–charge SCs of the NGS, MLG, GEG and GNS electrodes are 1859.6/832.4, 840.5/269.1, 621.5/128.5, and 1260.1/571.4 mA h g^{-1}, respectively. The first Coulombic efficiency (CE) of the NGS electrode is 44.8%, which is roughly equal to that of GNS (45.3%), and much higher than those of MLG (32.0%) and GEG (20.7%). Nevertheless, the first CE of NGS is lower than that of commercial graphite, it could be attributed mainly to the formation of a solid electrolyte interphase (SEI) film on graphene sheets[45] and the irreversible reactions of the lithium ion with the in-plane graphitic nitrogen sites or other undesirable dopants,[35] and some strategies could be adopted to boost the first efficiency.[35,36,61,62] Similar to the typical nanosized carbonaceous materials,[5,15,45] the slopes of the first discharge curves started from 3.0 V, without distinct potential plateaus. During the charge process, for MLG and GNS, the slopes started approximately from 1.2 V (*vs.* Li/Li^+) and have large SCs below 1.0 V with a distinguishable plateau, corresponding to the Li^+ deintercalation from graphene layers.[5,63,64] Whereas, the charge profiles of the NGS displayed appreciable voltage hysteresis, indicating that the extraction of Li^+ from the slit-shaped micropore has to go through the "way" of graphene crystallites, in which the inserted lithium ions were removed

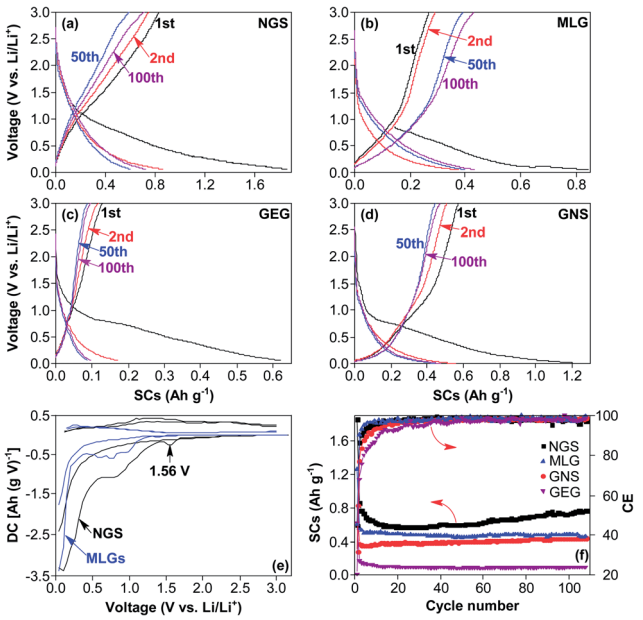

Fig. 7 Electrochemical characterization of a half-cell composed of the graphene electrode and Li over the voltage range 0.05–3.0 V *vs.* Li/Li^+ at a current density of 100 mA g^{-1}. Charge–discharge profiles for the 1st, 2nd, 50th, and 100th cycle for (a) NGS, (b) MLG, (c) GEG and (d) GNS; (e) initial 2 cycles charge–discharge differential capacity *versus* voltage plots (d*Q*/d*V*) of the NGS and MLG and (f) cyclic performances and CE.

from the entire voltage range, and without distinct potential plateaus in charge curves. Details of the first charge–discharge processes for NGS and MLG electrodes could be reflected as peaks in the differential capacity *versus* voltage plots, several reduction and oxidation peaks are clearly observed for the NGS and MLG (Fig. 7e), respectively. According to the reaction mechanism proposed in the previous studies,[4,45] the peaks at 0.5–1.0 V in the discharge process are mainly caused by the SEI formation, *i.e.*, the reaction of lithium ions with the active sites and decomposition of electrolytes on the surface of graphene electrodes, which are the main reasons of the initial irreversible capacity. These peaks can be typically enhanced by increasing the SSA and structural disorder of the electrode materials, and thus, an enhanced peak of the NGS can be attributed to the larger surface-to-volume ratio and surface electrochemical reactivity. In addition, compared with that of the MLG, an extra discharge peak appeared around 1.56 V for the NGS electrode, which practically disappeared after the first cycle, probably due to the consumption of lithium ions in the irreversible reaction with the graphitic nitrogen and/or other impurities.[25–35]

For the subsequent cycles, it is generally believed that the discharge capacity below 0.5 V (*vs.* Li/Li^+) is due to lithium insertion into the graphene layers (lithium insertion capacity, LIC), and yet the capacity above 0.5 V (*vs.* Li/Li^+) could be associated with the Faradic capacitance resulting from the adsorption of Li^+ on pyridinic or pyrrolic defect structures.[4,5,25,64,65] As shown in Table 3, the LIC of NGS (377.7 mA h g^{-1}) was marginally higher than that of the GNS electrode (359.8 mA h g^{-1}). Despite the close SSA, however, comparing

Table 3 FC, LIC and TC of the 100th cycle discharge process for NGS, MLG, GEG and GNS electrodes at 100 mA g^{-1}

	Capacity (mA h g^{-1})			
Sample	FC	LIC	TC	FC/TC (%)
NGS	349.4	377.7	727.1	48.05
MLG	182.8	252.2	435	42.02
GEG	45	52.6	97.6	46.11
GNS	118	359.8	477.8	24.70

with that of the GNS electrode, the NGS electrode delivered a much higher Faradic capacity (FC) of 349.4 mA h g^{-1}, about 3 times that of the GNS electrode (118 mA h g^{-1}), and it is also the main contribution to the high total capacity (TC) of the NGS, manifesting the outstanding interfacial properties of the NGS. Fig. 7f shows the cycling performance of the NGS, MLG, GEG and GNS electrodes at a current density of 100 mA g^{-1} for 108 cycles. It is worth noting that the NGS electrode presented a much improved discharge capacity, which was gradually increased after 30 cycles, and 770.8 mA h g^{-1} was achieved after 108 cycles, nearly two times that of the MLG (441 mA h g^{-1}) or GNS (460.5 mA h g^{-1}), suggesting excellent cycling performance of the NGS electrode. It is speculated that the curious phenomenon of gradually increased capacity might owe to the conversion of graphitic nitrogen into the pyridinic structure and/or the proliferation of in-plane defects during the electrochemical cycling.

To further investigate the electrochemical performance of the NGS, rate capabilities and high rate cycling performances of the NGS electrode were examined (Fig. 8). An excellent high rate capability was determined for NGS, a charge capacity of 666 mA

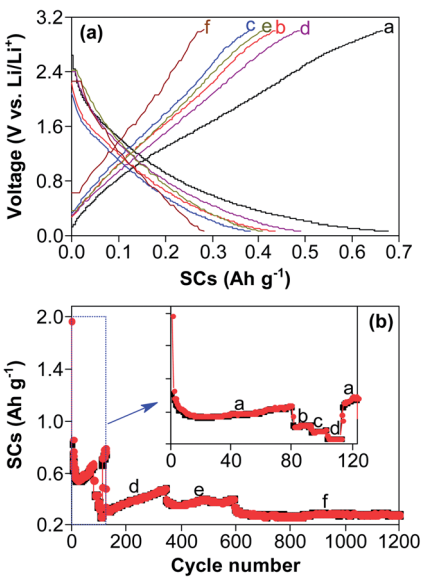

Fig. 8 Rate capabilities and high rate cycling performances of the NGS electrode at various current densities over the voltage range 0.05–3.0 V *vs.* Li/Li^+. (A) Charge–discharge profiles and (B) high rate cycling performances. (a) 100 mA g^{-1}, (b) 500 mA g^{-1}, (c) 1000 mA g^{-1}, (d) 2500 mA g^{-1}, (e) 5000 mA g^{-1}, and (f) 10 000 mA g^{-1}.

h g^{-1} was obtained after the first 80 cycles at a low current density of 100 mA g^{-1}, and then it slowly reduced to 441.2, 380.5, and 275.2 mA h g^{-1} at current densities of 500, 1000, and 2500 mA g^{-1}, respectively. A superior capacity of 771.3 mA h g^{-1} could be obtained in the 121st cycle when the current density was reduced back to 100 mA g^{-1}. And, as noted above, while the electrode was cycled at 2500 mA g^{-1} again, the reversible capacity could recover to 339.2 mA h g^{-1}, afterwards, it could increase to 486.3 mA h g^{-1} after 344 cycles. Moreover, the ability of the NGS electrode to retain the storage capacity at very high rates, as well as a fascinating high rate cyclic performance, is what should be noted. Over 43% of the storage capacity was retained for a 100-fold increase in rate, *i.e.*, a reversible capacity of 333 mA h g^{-1} (595th cycle) at a current density as high as 10 000 mA g^{-1} (corresponding to a discharge or charge time of *ca.* 120 s) was achieved, significantly higher than those of the graphene-based electrodes reported previously. Furthermore, this capacity is retained at 280.6 mA h g^{-1} even after 1200 cycles, attaining a capacity retention of 84.3% at the current density of 10 000 mA g^{-1} from 595th to 1200th cycle. To the best of our knowledge, such an excellent high-rate performance is superior to all existing graphene-based materials reported for LIBs.[6,24,29,30,33,38,41,64,66–69] The discharge FC, LIC and TC of the NGS at various current densities are shown in Table 4. When cycled at a low rate, the LIC and TC are roughly equivalent. With an increasing current density, the LIC decreased significantly as expected, yet the FC tardily decreased, and FC/TC increased gradually, when cycled at the high current density of 10 000 mA g^{-1}, and the FC contributed to most of the TC (70.28%), corresponding to the rapid lithium adsorption in the NGS.

CV profiles (Fig. 9) at different scan rates were processed to survey the electrochemical cycling behaviors of the NGS and MLG electrodes. CV curves of the MLG electrode exhibit a pair of peaks located below 0.5 V, corresponding to the intercalation and deintercalation processes of lithium ions. Nevertheless, distinct from that of the MLG, sweeping at 1 mV s^{-1}, the CV curve of the NGS electrode displayed typical capacitive behavior along the potential range of 0.5–3 V, corresponding to the Li^+ adsorption in trimerized pyridine-type nitrogen sites, and a higher cathodic current peak at 0 V which is related to Li^+ intercalation in the graphitic structure.[23,25,34–36,70] When the scan rate was increased, it is intriguing to see that the shape of the CV curve, over the entire potential range, was transformed into a quasi-rectangular one gradually, and correspondingly, the lithium intercalation peak was substantially decreased, indicating that the reactions of Li^+ with the pyridinic structure were predominant processes for the high-capacity of the NGS at high rate cycling, and the lithium storage behavior in the NGS was more like an ideal supercapacitor.

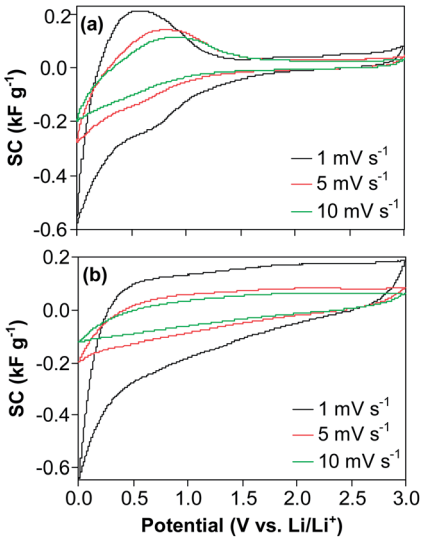

Fig. 9 CV curves of the (a) MLG and (b) NGS electrodes in the voltage range of 0–3 V at 1, 5 and 10 mV s^{-1} *vs.* Li/Li^+.

To understand the excellent electrochemical performance, a schematic illustration (Fig. 10) for the lithium-storage mechanism of the NGS was proposed. The NGS was finally obtained after removing the GCN template from GEG, and it is considered that nitrogen atoms were doped into the graphene lattice dominantly in the form of the pyridinic structure. The pyridinic dopant could enlarge the binding energies of the lithium atom with graphene planes and simultaneously lower the energy barrier of Li^+ diffusion. Thus more Li^+ ions could be embedded on the NGS plane and consequently exhibited increased storage capacity.[25,34,36] Furthermore, defects including the intergranular cavities and the in-plane vacancies offer the large electrolyte contact area and also enable lithium penetration across the

Table 4 FC, LIC and TC of the NGS electrode at different current densities

Current density (mA g^{-1})	Capacity (mA h g^{-1})			FC/TC (%)	Cycle number
	FC	LIC	TC		
100	330.6	348.6	679.2	48.67	80
500	233.9	201.9	435.8	53.67	92
1000	211.1	170.5	381.6	55.32	102
2500	276.5	212.4	488.9	56.56	344
5000	247.2	162.5	409.7	60.34	594
10 000	197.2	83.4	280.6	70.28	1200

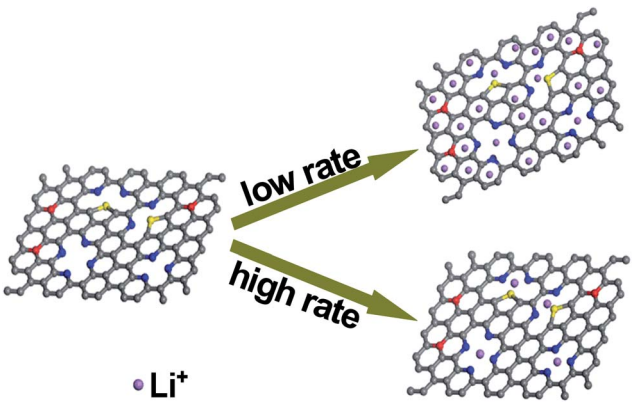

Fig. 10 Schematic illustration for the lithium-storage mechanism of the NGS.

graphene layers,[23] which results in a significant reduction of the Li^+ diffusion path and thus can expedite ion transport, exhibiting superior rate capabilities and high rate cycling performances.

4 Conclusions

A facile bottom-up strategy was developed to fabricate NGSs from glucose by using a sacrificial template synthesis method. It was found that three main types of nitrogen dopants (pyridinic nitrogen, pyrrolic nitrogen and graphitic nitrogen) were introduced into the graphene lattice, and an inimitable microporous structure of NGSs with a high SSA of 504 $m^2 g^{-1}$ was obtained. Particularly, with hybrid features of lithium ion batteries and Faradic capacitors at a low rate and features of Faradic capacitors at a high rate, the NGS presented a superior lithium storage performance. During electrochemical cycling, the NGS electrode afforded an enhanced reversible capacity of 832.4 mA h g^{-1} at 100 mA g^{-1} and an excellent cycling stability of 750.7 mA h g^{-1} after 108 cycles. Furthermore, an astonishing rate capability of 333 mA h g^{-1} at 10 000 mA g^{-1} and a high rate cycle performance of 280.6 mA h g^{-1} even after 1200 cycles were also achieved, highlighting the significance of nitrogen doping on the maximum utilization of graphene-based materials for advanced lithium storage. More importantly, the developed bottom-up synthesis strategy and the obtained unique nanoarchitectures are envisaged to pave the way toward the design and fabrication of novel graphene-based composites with enhanced properties for high energy and high power lithium storage and/or other applications.

Acknowledgements

The authors acknowledge financial support from the Fund from the National Natural Science Foundation of China for Innovative Research Group (Grant 51221462), the Jiangsu Ordinary University Graduate Innovative Research Programs (CXZZ12_0943, CXZZ13_0952), Jiangsu Planned Projects for Postdoctoral Research Funds (1201030C), and the Priority Academic Program Development of Jiangsu Higher Education Institutions.

References

1 X. Zhao, C. M. Hayner, M. C. Kung and H. H. Kung, *Adv. Energy Mater.*, 2011, **1**, 1079–1084.
2 K. S. Novoselov, A. K. Geim, S. V. Morozov, D. Jiang, Y. Zhang, S. V. Dubonos, I. V. Grigorieva and A. A. Firsov, *Science*, 2004, **306**, 666–669.
3 S. Sattayasamitsathit, Y. Gu, K. Kaufmann, W. Jia, X. Xiao, M. Rodriguez, S. Minteer, J. Cha, D. B. Burckel, C. Wang, R. Polsky and J. Wan, *J. Mater. Chem. A*, 2013, **1**, 1639–1645.
4 G. X. Wang, X. P. Shen, J. Yao and J. Park, *Carbon*, 2009, **47**, 2049–2053.
5 E. J. Yoo, J. Kim, E. Hosono, H. S. Zhou, T. Kudo and I. Honma, *Nano Lett.*, 2008, **8**, 2277–2282.
6 X. Zhao, C. M. Hayner, M. C. Kung and H. H. Kung, *ACS Nano*, 2011, **5**, 8739–8749.
7 Z. S. Wu, G. M. Zhou, L. C. Yin, W. Ren, F. Li and H. M. Cheng, *Nano Energy*, 2012, **1**, 107–131.
8 L. L. Tian, Q. C. Zhuang, J. Li, C. Wu, Y. L. Shi and S. G. Sun, *Electrochim. Acta*, 2012, **65**, 153–158.
9 S. Yang, X. Feng, S. Ivanovici and K. Müllen, *Angew. Chem., Int. Ed.*, 2010, **49**, 8408–8411.
10 S. M. Paek, E. Yoo and I. Honma, *Nano Lett.*, 2009, **29**, 72–75.
11 H. L. Wang, L. F. Cui, Y. Yang, H. S. Casalongue, J. T. Robinson, Y. Y. Liang, Y. Cui and H. J. Dai, *J. Am. Chem. Soc.*, 2010, **132**, 13978–13980.
12 L. L. Tian, X. Y. Wei, Q. C. Zhuang, C. Wu, R. L. Xie, Z. M. Zong, Y. L. Cui and S. G. Sun., *Nano*, 2013, **8**, 1350068.
13 L. L. Tian, X. Y. Wei, Q. C. Zhuang, Z. M. Zong and S. G. Sun., *Acta Chim. Sin.*, 2013, **71**, 1270–1274.
14 S. Yang, Y. Gong, Z. Liu, Z. Liang, D. P. Hashim, L. Ma, R. Vajtai and P. M. Ajayan, *Nano Lett.*, 2013, **13**, 1596–1601.
15 D. Y. Pan, S. Wang, B. Zhao, M. H. Wu, H. J. Zhang, Y. Wang and Z. Jiao, *Chem. Mater.*, 2009, **21**, 3136–3142.
16 E. Pollak, B. S. Geng, K. J. Jeon, I. T. Lucas, T. J. Richardson, F. Wang and R. Kostecki, *Nano Lett.*, 2010, **10**, 3386–3388.
17 C. Uthaisar and V. Barone, *Nano Lett.*, 2010, **10**, 2838–2842.
18 E. Lee and K. A. Persson, *Nano Lett.*, 2012, **12**, 4624–4628.
19 N. A. Kaskhedikar and J. Maier, *Adv. Mater.*, 2009, **21**, 2664–2680.
20 M. H. Liang and L. J. Zhi, *J. Mater. Chem.*, 2009, **19**, 5871–5878.
21 A. Ferre-Vilaplana, *J. Phys. Chem. C*, 2008, **112**, 3998–4004.
22 C. Ataca, E. Akturk, S. Ciraci and H. Ustunel, *Appl. Phys. Lett.*, 2008, **93**, 043123.
23 F. Yao, F. Günes, H. Q. Ta, S. M. Lee, S. J. Chae, K. Y. Sheem, C. S. Cojocaru, S. S. Xie and Y. H. Lee, *J. Am. Chem. Soc.*, 2012, **134**, 8646–8654.
24 Z. S. Wu, W. Ren, L. Xu, F. Li and H. M. Cheng, *ACS Nano*, 2011, **5**, 5463–5471.
25 C. Ma, X. Shao and D. Cao, *J. Mater. Chem.*, 2012, **22**, 8911–8915.
26 Y. Mao, H. Duan, B. Xu, L. Zhang, Y. Hu, C. Zhao, Z. Wang, L. Chen and Y. Yang, *Energy Environ. Sci.*, 2012, **5**, 7950–7955.
27 L. S. Panchakarla, K. S. Subrahmanyam, S. K. Saha, A. Govindaraj, H. R. Krishnamurthy, U. V. Waghmare and C. N. R. Rao, *Adv. Mater.*, 2009, **21**, 4726–4730.
28 Z. Jin, J. Yao, C. Kittrell and J. M. Tour, *ACS Nano*, 2011, **5**, 4112–4117.
29 A. L. Reddy, A. Srivastava, S. R. Gowda, H. Gullapalli, M. Dubey and P. M. Ajayan, *ACS Nano*, 2010, **4**, 6337–6342.
30 X. Li, D. Geng, Y. Zhang, X. Meng, R. Li and X. Sun, *Electrochem. Commun.*, 2011, **13**, 822–825.
31 D. Geng, S. Yang, Y. Zhang, J. Yang, J. Liu, R. Li, T. K. Sham, X. Sun, S. Ye and S. Knights, *Appl. Surf. Sci.*, 2011, **257**, 9193–9198.
32 H. B. Wang, C. J. Zhang, Z. H. Liu, L. Wang, P. Han, H. Xu, K. Zhang, S. Dong, J. Yao and G. Cui, *J. Mater. Chem.*, 2011, **21**, 5430–5434.

33 D. H. Deng, X. L. Pan, L. Yu, Y. Cui, Y. P. Jiang, J. Qi, W. X. Li, Q. Fu, X. C. Ma, Q. K. Xue, G. Q. Sun and X. H. Bao, *Chem. Mater.*, 2011, **23**, 1188–1193.
34 K. X. Kong and W. Q. Chen, *Phys. Chem. Chem. Phys.*, 2013, **15**, 12982–12987.
35 G. M. Veith, L. Baggetto, L. A. Adamczyk, B. Guo, S. S. Brown, X. G. Sun, A. A. Albert, J. R. Humble, C. E. Barnes, M. J. Bojdys, S. Dai and N. J. Dudney, *Chem. Mater.*, 2013, **25**, 503–508.
36 Y. X. Yu, *Phys. Chem. Chem. Phys.*, 2013, **15**, 16819–16827.
37 H. Wang, M. Xie, L. Thia, A. Fisher and X. Wang, *J. Phys. Chem. Lett.*, 2014, **5**, 119–125.
38 T. Hu, X. Sun, H. Sun, G. Xin, D. Shao, C. Liu and J. Lin, *Phys. Chem. Chem. Phys.*, 2014, **16**, 1060–1066.
39 Y. Shao, S. Zhang, M. H. Engelhard, G. Li, G. Shao, Y. Wang, J. Liu, I. A. Aksay and Y. Lin, *J. Mater. Chem.*, 2010, **20**, 7491–7496.
40 D. Ding, Z. L. Song, Z. Q. Cheng, W. N. Liu, X. K. Nie, X. Bian, Z. Chen and W. Tan, *J. Mater. Chem. A*, 2014, **2**, 472–477.
41 X. Zhou, J. Bao, Z. Dai and Y. G. Guo, *J. Phys. Chem. C*, 2013, **117**, 25367–25373.
42 D. Long, W. Li, L. Ling, M. Jin, I. Mochida and S. H. Yoon, *Langmuir*, 2010, **26**, 16096–16102.
43 X. H. Li, S. Kurasch, U. Kaiser and M. Antonietti, *Angew. Chem., Int. Ed.*, 2012, **51**, 9689–9692.
44 X. Wang, K. Maeda, A. Thomas, K. Takanabe, G. Xin, J. M. Carlsson, K. Domen and M. Antonietti, *Nat. Mater.*, 2008, **8**, 76–80.
45 L. L. Tian, Q. C. Zhuang, J. Li, Y. L. Shi, J. P. Chen, F. Lu and S. G. Sun, *Chin. Sci. Bull.*, 2011, **56**, 3204–3212.
46 S. W. Bian, Z. Ma and W. G. Song, *J. Phys. Chem. C*, 2009, **113**, 8668–8672.
47 K. Parvez, S. Yang, Y. Hernandez, A. Winter, A. Turchanin, X. Feng and K. Müllen, *ACS Nano*, 2012, **11**, 9541–9550.
48 P. Niu, L. Zhang, G. Liu and H. M. Cheng, *Adv. Funct. Mater.*, 2012, **22**, 4763–4770.
49 F. Goettmann, A. Fischer, M. Antonietti and A. Thomas, *Angew. Chem., Int. Ed.*, 2006, **45**, 4467–4471.
50 H. Yan, Y. Chen and S. Xu, *Int. J. Hydrogen Energy*, 2012, **37**, 125–133.
51 L. Qu, Y. Liu, J. B. Baek and L. Dai, *ACS Nano*, 2010, **4**, 1321–1326.
52 J. Sun, H. Liu, X. Chen, D. G. Evans, W. Yang and X. Duan, *Chem. Commun.*, 2012, **48**, 8126–8128.
53 Z. Luo, S. Lim, Z. Tian, J. Shang, L. Lai, B. MacDonald, C. Fu, Z. Shen, T. Yu and J. Lin, *J. Mater. Chem.*, 2011, **21**, 8038–8044.
54 P. Lian, X. Zhu, S. Liang, Z. Li, W. Yang and H. Wang, *Electrochim. Acta*, 2010, **55**, 3909–3914.
55 Y. Cui, J. Zhang, G. Zhang, J. Huang, P. Liu, M. Antonietti and X. Wang, *J. Mater. Chem.*, 2011, **21**, 13032–13039.
56 Y. C. Liu and D. N. Lu, *Plasma Chem. Plasma Process.*, 2006, **26**, 119–126.
57 C. Yuan, W. Chen and L. Yan, *J. Mater. Chem.*, 2012, **22**, 7456–7460.
58 J. Song, T. Xu, M. L. Gordin, P. Zhu, D. Lv, Y. B. Jiang, Y. Chen, Y. Duan and D. Wang, *Adv. Funct. Mater.*, 2014, **24**, 1243–1250.
59 A. Thomas, A. Fischer, F. Goettmann, M. Antonietti, J. O. Müller, R. Schlögl and J. M. Carlsson, *J. Mater. Chem.*, 2008, **18**, 4893–4908.
60 F. Dong, L. Wu, Y. Sun, M. Fu, Z. Wu and S. C. Lee, *J. Mater. Chem.*, 2011, **21**, 15171–15174.
61 D. Aurbach, K. Gamolsky, B. Markovsky, Y. Gofer, M. Schmidt and U. Heider, *Electrochim. Acta*, 2002, **47**, 1423–1439.
62 Z. S. Wu, L. Xue, W. Ren, F. Li, L. Wen and H. M. Cheng, *Adv. Funct. Mater.*, 2012, **22**, 3290–3297.
63 P. Guo, H. Song and X. Chen, *Electrochem. Commun.*, 2009, **11**, 1320–1324.
64 Z. Jiang, B. Pei and A. Manthiram, *J. Mater. Chem. A*, 2013, **1**, 7775–7781.
65 R. Yazami and M. Deschamps, *J. Power Sources*, 1995, **54**, 411–415.
66 D. A. C. Brownson, D. K. Kampouris and C. E. Banks, *J. Power Sources*, 2011, **196**, 4873–4885.
67 S. Han, D. Wu, S. Li, F. Zhang and X. Feng, *Small*, 2013, **9**, 1173–1187.
68 Y. Fang, Y. Lv, R. Che, H. Wu, X. Zhang, D. Gu, G. Zheng and D. Zhao, *J. Am. Chem. Soc.*, 2013, **135**, 1524–1530.
69 R. Mukherjee, A. V. Thomas, A. Krishnamurthy and N. Koratkar, *ACS Nano*, 2012, **6**, 7867–7878.
70 E. Paek, A. J. Pak, K. E. Kweon and G. S. Hwang, *J. Phys. Chem. C*, 2013, **117**, 5610–5616.